

# AARTFAAC discovery of extreme-fluence pulses from PSR B0950+08

Mark Kuiack,<sup>1\*</sup> Ralph A.M.J. Wijers,<sup>1</sup> Antonia Rowlinson,<sup>1,2</sup>  
Aleksandar Shulevski,<sup>1</sup> Folkert Huizinga,<sup>1</sup> Gijs Molenaar,<sup>3</sup> Peeyush Prasad,<sup>1</sup>

<sup>1</sup> Anton Pannekoek Institute for Astronomy, University of Amsterdam, Science Park 904, 1098 XH, Amsterdam, The Netherlands

<sup>2</sup> ASTRON, Netherlands Institute for Radio Astronomy, Oude Hoogeveensedijk 4, 7991 PD Dwingeloo, The Netherlands

<sup>3</sup> Department of Physics and Electronics, Rhodes University, PO Box 94, Grahamstown, 6140, South Africa

Accepted XXX. Received YYY; in original form ZZZ

## ABSTRACT

Here we report on the detection of extreme-fluence pulses (EFP) from PSR B0950+08 with the Amsterdam-Astron Radio Transient Facility And Analysis Center (AARTFAAC), a parallel transient detection instrument operating as a subsystem of the LOW Frequency ARray (LOFAR). During processing of our Northern Hemisphere survey for low frequency (58.3 and 61.8 MHz) radio transients, a sample of 275 pulses with fluences ranging from 42k to 177k Jy ms were detected in one-second snapshot images. The brightest pulses are more than two orders of magnitude brighter than those previously reported at 42 and 74 MHz. Although the power-law pulse-energy distribution index agrees well with the previous results, the average rate of EFPs is much higher. Given the number of EFPs observed, and the power-law index of the pulse-fluence distribution at high fluence, a single power-law cannot be extended to the typical pulse population. Activity was found to be highly variable, with only two three-hour observations accounting for nearly half of the pulses detected in the 96 hours surveyed. The rate of EFPs varied from 0 to 30 detected per hour between consecutive days of observation. However, no clustering was observed within a single active 3-hour span. The spectra appear intrinsically structured with narrow band emission, confined, at times, within 195.3 kHz sub-bands, and dynamic, with the pulse spectra changing on timescale of ~10 minutes. This narrow emission bandwidth provides strong evidence that the EFPs are intrinsically higher energy, rather than being magnified by propagation effects.

**Key words:** pulsars:general – pulsars:individual(B0950+08) – radio continuum:transients

## 1 INTRODUCTION

Within a year of the discovery of the first pulsar (Hewish et al. 1968), extreme emission phenomena, later argued to be caused by a completely different emission mechanism and called “giant pulses,” were also discovered from the Crab pulsar (Staelin & Reifenstein 1968). Although a pulsar’s rotation period is extremely regular and can be measured with great precision, the brightness of any given pulse can be highly variable. This observed variability must either be the result of propagation effects or an intrinsic fluctuation in the mechanism by which the coherent radio pulses are being generated.

According to the ATNF Pulsar Catalogue<sup>1</sup>, currently there are 2659 known pulsars (Manchester et al. 2005), of which only 24 have been observed to produce giant pulses (Kazantsev & Potapov 2018). It should be noted, however, that some ambiguity exists in the definition of a giant pulse, and therefore the name may capture a variety of physical phenomena. Kuzmin (2007) defines giant pulses by applying a statistical criterion on the population: “above a certain threshold” pulse fluxes exhibit a power-law rather than log-normal distribution. However, Kazantsev & Potapov (2018) illustrate smooth transitions between the log-normal distri-

\* E-mail: m.j.kuiack@uva.nl

<sup>1</sup> <http://www.atnf.csiro.au/research/pulsar/psrcat/>

bution of typical pulses<sup>2</sup> and “giant pulses” for 8 pulsars. A useful description is given by Cairns (2004), who defined a giant pulse as a pulse whose total integrated flux is greater than 10 times the mean-intensity profile (MIP), as opposed to giant micro-pulses, which achieve a peak flux greater than 10 times, but whose pulse integrated flux is less than 10 times, resulting from a much narrower pulse width. While the number 10 remains arbitrary, the distinction in pulse flux distribution shape suggests a different emission mechanism may be at work.

Regardless, it is clear that pulsars are capable of producing coherent pulsed radio emission via a variety of mechanisms. Giant pulses observed by Kazantsev & Potapov (2018) are much narrower in time than the averaged pulse profile, can appear irregularly distributed across the pulse phase (Kazantsev et al. 2019), and may be coincident with high energy emission (Bilous et al. 2015).

It has also been shown that the fluence of a pulsar’s MIP can vary by up to an order of magnitude over the course of a few days. This long term variability in the MIP intensity is attributed to propagation effects, such as refractive or diffractive interstellar scintillation, RISS and DISS respectively (Gupta et al. 1993; Wang et al. 2005).

Additionally, Main et al. (2018) recently showed that some extra luminous pulses originating from PSR B1957+20 are in fact the result of extreme lensing, caused by an intra-binary ionized plasma resulting from material blown off of the stellar companion, by the pulsar wind. These are described as brighter typical pulses, achieving magnification factors up to 30 times the MIP. These lensed pulses only appear at specific phases of the binary orbit, in contrast to the many giant pulses which were also recorded throughout the same observation. Therefore, current literature suggests it is difficult to say whether a single bright pulse is simply the bright tail of the typical energy distribution, typical pulses extrinsically magnified by the medium through which the pulses propagate, or a distinct phenomenon produced by a completely different mechanism.

Nonetheless, the different characteristics of giant pulses: Power-law vs Gaussian flux statistics (Wang et al. 2019), tendency towards narrower pulse profiles, alternation between main pulse and inter-pulse phase (Main & van Kerkwijk 2018), variable dispersion measure (DM) (McKee et al. 2019), suggest strongly that pulsars are capable of producing coherent radio emission via a diverse set of mechanisms.

Here we report on the detection of extreme-fluence pulses (EFPs), with fluence ratios greater than 1000 times the MIP, from the pulsar B0950+08 by the Amsterdam-ASTRON Radio Transient Facility And Analysis Centre (AARTFAAC). AARTFAAC is a radio transient survey project attached to the LOw-Frequency ARray (LOFAR), whose aim is to search for bright (10s of Jy), brief (seconds to minutes timescale), transient events around 60 MHz (Prasad et al. 2016).

PSR B0950+08 is an interesting pulsar both because of the highly variable magnitude of its MIP (Gupta et al. 1993), as well as its production of giant pulses (Singal 2001). Additionally, this pulsar has been of particular interest due to

it being one of the lowest DM,  $\sim 3 \text{ pc cm}^{-3}$ , and closest pulsars. At  $262 \pm 5 \text{ pc}$  (Brisken et al. 2002), it is just beyond the wall of the Local Bubble, a region of reduced density of the interstellar medium (ISM) surrounding the Sun (Spangler 2009).

In Section 2 we describe our instrument, observations, and data processing methodology. We then report details of the observed pulses and population statistics in Section 3. Next, in Section 4 we discuss evidence which might characterize the origin of the extremely luminous pulses. Finally, some conclusions are made in Section 5.

## 2 INSTRUMENT AND OBSERVATIONS

AARTFAAC is an all-sky, radio telescope experiment, designed to survey the Northern Hemisphere for bright low frequency transient events which evolve on timescales from one-second to several minutes (Prasad et al. 2016). It operates as a parallel back-end on the Low Frequency Array, LOFAR (van Haarlem et al. 2013). The radio signals are split directly from the 288 inverted V antennas, which make up the six low band antenna (LBA) stations of the “superterp,” and processed by dedicated correlators, and calibration and imaging servers. The largest baseline on the superterp is 300 meters, resulting in an angular resolution of 60 arcmin. Accessing the signal directly from the dipoles provides a full sky field of view. However, due to ground based radio frequency interference (RFI), and a significant drop in sensitivity towards the horizon, the detection region for transients is set to 50 degrees from zenith. This allows for the detection of 30–50 persistent sources, per second, across the field of view, with a significance of  $5\sigma$  ( $\sim 50 \text{ Jy}$  during typical conditions).

We observe simultaneously with any regularly scheduled LOFAR-LBA, or during “filler time” when no observation has been scheduled. Therefore, the archived data sets vary in length and are spaced irregularly in time, with LST matched observations over consecutive days occurring rarely in the schedule. Although LBA and filler time observations represent a minority of the total scheduled LOFAR observations, the AARTFAAC archive has accumulated over 1100 hours of observations between August 2016 and September 2019. The complete set of observations used in this work consists of 96 hours spanning 2016-09-07 to 2019-05-21. The date of these observations, as well as the rate of pulses detected per hour, are illustrated in Fig. 1.

The data were recorded as 16 separate, 195.3 kHz bandwidth, calibrated sub-bands, integrated in 1 second blocks of time. Visibility calibration is described fully in (Prasad et al. 2014), but put simply, the brightest sources: Cassiopeia A, Cygnus A, Taurus A, Virgo A, and the Sun are subtracted with single component Gaussian models, and the large scale diffuse Galactic emission is reduced by imposing a minimum baseline length of  $10\lambda$ , 50 meters at 60 MHz.

The blind search for radio transients is done by first generating two all-sky images,  $1024 \times 1024$  pixels, each second, with a bandwidth of 1.5 MHz, centered at 58.3 and 61.8 MHz, near the peak of the LBA sensitivity. The images are then processed by the LOFAR Transient Pipeline

<sup>2</sup> Commonly referred to as average pulses (APs) in pulsar literature.

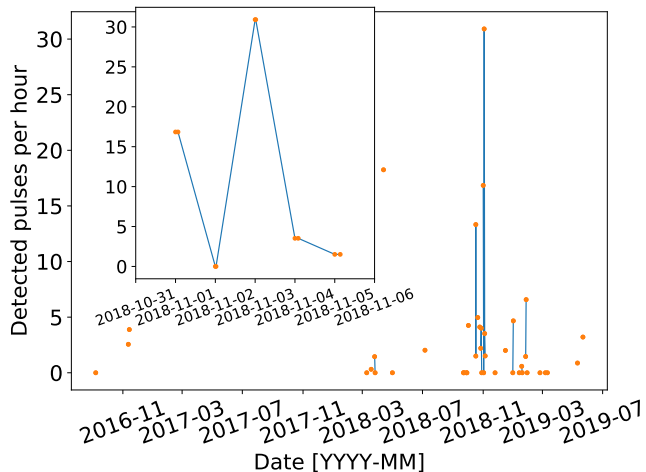


**Figure 1.** The rate of pulses detected over the course of our observations. The observation start time is marked with an orange dot; observations within 24 hours are connected with a blue line. The rate varies greatly from day to day. The inset plot shows the high day to day variation rate of pulses, indicating that the activity correlation timescale is less than 1 day.

(TraP; Swinbank et al. 2015, and references therein)<sup>3</sup>, which ingests an image set from an AARTFAAC observation, performs source finding in each image, associates sources across images, while calculating detection significance and variability statistics.

Although integrating the 16 sub-bands into two 8 sub-band images sacrifices some instantaneous sensitivity relative to a single 16 sub-band image, it allows for the immediate removal of many types of RFI, which typically manifest as very bright narrow band sources. Additionally, it allows the ability to discern side-lobe peaks, whose position is frequency dependent. Therefore, two criteria are imposed which filter a significant fraction of transient candidates; firstly, the source must be detected at  $5\sigma$  in both images, set as the detection threshold in TraP, and secondly, it must achieve a significance of  $8\sigma$  or greater in at least one image, at some point during the observation, a criterion applied when querying the source database.

## 2.1 Flux scaling

The flux density scaling solution for each image is calculated by comparing the extracted flux densities for all sources in the field of view, detected with a signal-to-noise ratio greater than  $5\sigma$ , with the values previously measured in the AARTFAAC Northern hemisphere catalogue at 60 MHz (Kuiack et al. 2018). The scaling solution in a single image is computed independently by linear least-squares fit of the extracted source flux densities to their catalogued reference values. Utilizing the maximal number of high significance sources across the entire visible sky allows for a much more stable flux density scaling solution which is not strongly influenced by the variability in any single source, or sky region.

<sup>3</sup> <https://github.com/transientskp/tkp>

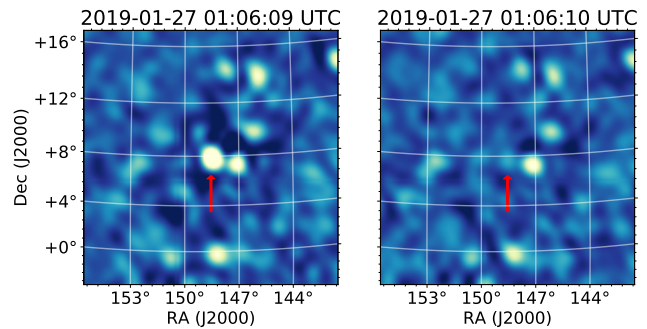


**Figure 2.** Example image stamps showing one of the brightest pulses detected, with a fluence of  $177 \pm 53$  Jy s (left), while the background in the next frame is  $34 \pm 25$  Jy s (right). The FWHM of the AARTFAAC PSF is 60 arc minutes. The source immediately adjacent is 3C 227, a Seyfert 1 galaxy with a flux density of  $113.7 \pm 0.1$  Jy at 60 MHz, in the AARTFAAC catalogue.

The validity of the flux scaling is measured by comparing the extracted flux densities of the AARTFAAC catalogue sources to their catalogued value. There is no appreciable systematic offset ( $<1\%$ ), and the average uncertainty is 30%. This level of uncertainty in the measured flux density of an individual source from a single 1 second, 1.5 MHz integrated image is typical, with the main contributor to the uncertainty being ionospheric scintillation which, under normal conditions, modulates the brightness by 10 – 30%, on timescales of 10 – 20 minutes. 30% can therefore be used as a conservative estimate of the instantaneous uncertainty in a single AARTFAAC flux density measurement (Kuiack et al. 2018).

## 3 RESULTS

The signal from B0950+08 was originally detected as a transient candidate when analyzing the blind transient survey observation from 2018-11-01. Following the detection, we performed a search of the accumulated transient candidate database, at the location of B0950+08, for any signal previously detected but which did not satisfy the selection criteria outlined in Section 2. Additionally, observations stored in the visibility archive, with B0950+08 within the field of view, were prioritized for processing until a sufficient population of pulses were detected.

In total 275 pulses were detected in 96 hours of observations, see Fig. 1. The inset of the plot shows the rate of EFPs detected per hour, given that this is not a smoothly varying function across the consecutive days sampled it is clear that the timescale on which activity is correlated is less than 1 day.

The brightest pulse detected, with a fluence of  $177 \pm 53$  Jy s, is shown in Fig. 2.

### 3.1 Pulse fluence distribution

The statistical distribution of all pulses detected thus far shows striking similarity, in power-law index, to the population of giant pulses observed by Tsai et al. (2016) using the Long Wavelength Array (LWA), an instrument similar

**Table 1.** Comparison of the average and giant pulse parameters across the different observations. \* values are calculated assuming giant pulses have a width which is half of the mean-intensity profile (MIP). † values are calculated using parameters and interpolation between the LWA 42 and 74 MHz results.

Freq MHz	MIP width ms	MIP peak Jy	MIP fluence Jy ms	Max GP width ms	Max GP peak Jy	Max GP fluence Jy ms	Index	Source
112	15	2	32	5	15,240	81,240	-1.5	Smirnova (2012)
74	17.8	2.4	46.5	8.9*	69.6	659.4*	-5.06	Tsai et al. (2016)
61.8	20†	2.6†	55†	10*†	14,500*†	155,000	-4.82	This work
58.3	20†	2.6†	55†	10*†	16,700*†	177,000	-4.46	This work
42	25.6	2.8	76	12.8*	81.2	1106.4*	-4.09	Tsai et al. (2016)
39	30.5	1.5	48.7	19.6	42.3	829.08	-4.7	Tsai et al. (2015)

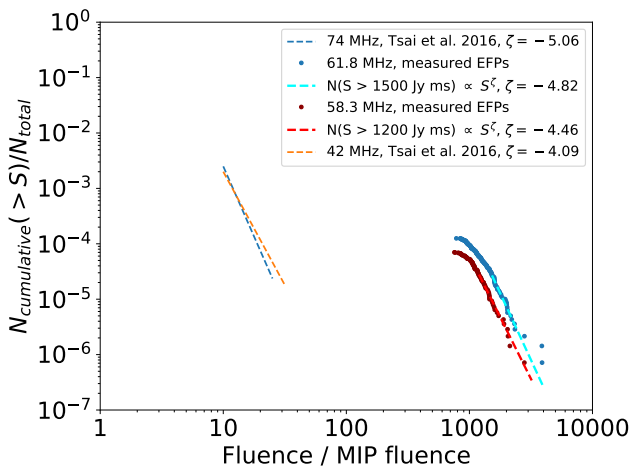


**Figure 3.** Cumulative fluence distributions from all of the pulses detected thus far in the AARTFAAC survey (red and blue dots), compared to estimations of the pulse fluence distributions fit at 74 and 42 MHz observed by LWA (dark blue and orange dashed lines). The power-law distributions are fit to pulses with fluence to MIP fluence ratios greater than 1500 at 61.8 MHz (light blue dashed line), and 1200 at 58.3 MHz (red dashed line), to avoid the effect of incompleteness in the sample at low fluences. Clearly the pulses detected by AARTFAAC represent a separate population of EFPs.

with design to AARTFAAC. Shown in Fig. 3: the power-law distribution indices at 42 and 74 MHz as measured by Tsai et al. (2016) agree well with our results at 58.3 and 61.8 MHz. However, the rate at which we are observing pulses is about ten orders of magnitude too high, given our pulses are 2 orders of magnitude brighter. The much higher rate at which pulses with an extremely large fluence are observed indicated this is clearly not merely the high fluence tail of the previously observed distribution.

Furthermore, extrapolating the distribution fit by Tsai et al. (2016), to the pulse to MIP fluence ratio of 1 yields a  $N_{\text{cumulative}}(> S)/N_{\text{total}} \approx 1$ . This is clear by extrapolating the dark blue and orange dashed lines in Fig. 3 which have been reproduced from Figure 6 in Tsai et al. (2016). This indicates that the pulses reported there could be drawn from a single distribution which extends below the detection threshold of LWA, suggesting that this is the bright tail of the

typical pulse distribution, similar to the cases reported by Kazantsev & Potapov (2018).

In contrast, extrapolating the pulse fluence distribution observed by AARTFAAC results in an pulse fluence to MIP fluence ratio of  $135 \pm 25$  when  $N_{\text{cumulative}}(> S)/N_{\text{total}} = 1$ . Given that the fluence ratio should be near or below 1 when the total number of pulses are accounted for, the tail of the pulse fluence distribution observed by AARTFAAC cannot be continuous with the typical pulse distribution. Therefore, clearly the pulses detected by AARTFAAC are a distinct population of pulses, distinct not only from the typical pulses, but also from the hitherto known GPs.

As described by Cairns (2004), the specific power-law index of the pulse flux distribution may give strong evidence to the nature of the emission mechanism. This suggests that both the LWA and AARTFAAC observations may be observing the same physical process, but offset by two orders of magnitude in fluence scale. In order to test the consistency of the fluence distribution we are observing, the populations of pulses from the two most active days, 2018-04-14 and 2018-10-17, as well as a collection of pulses from the less active days, were compared using a two sample KS tests, illustrated in Fig. 4. In order to ensure that variations in the sensitivity across multiple observations are not a confounding factor in the shape of the distributions, first a completeness limit was applied. We only compare pulses with a fluence greater than 68 Jy s, occurring when the  $5\sigma$  detection limit was less than 68 Jy s. We then compare the normalized cumulative fluence distributions from the two most active days and a sample of a similar size from days when only a few pulses were detected. Fig. 4 shows the similarity of the three populations. This is put more quantitatively using the two sample KS test. Here the null hypothesis, that the populations are drawn from the same distribution, is not rejected when comparing the less active days to each most active day.

### 3.1.1 Low fluence limit

In order to explore whether the low flux tail of this population is above the sensitivity limit of AARTFAAC, allowing a low end cut-off in the number of EFPs to be distinguished from the background, we performed a comparative analysis of the flux density distributions of the nearby background, and B0950+08.

Continuously monitoring fixed sky positions is a feature of the TraP, allowing forced flux measurements at the



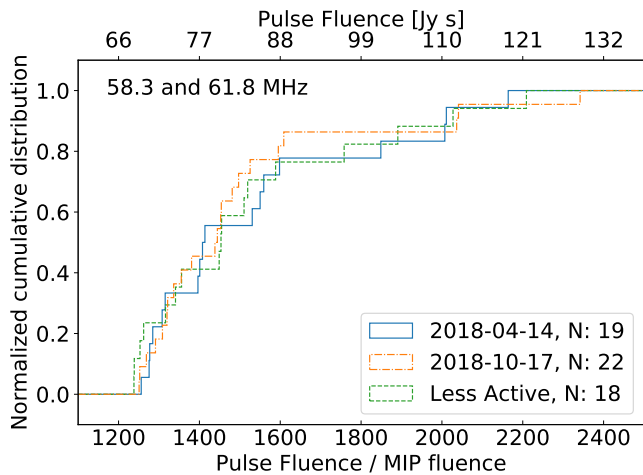


**Figure 4.** The cumulative fluence distributions of pulses from the two observations with the highest activity as well as a collected sample of pulses from observations when the pulsar appears less active.

position of target sources or background locations. The observation containing the most active time period was thus reprocessed with the TraP, resulting in a fully sampled light curve spanning the time, 18:00 to 22:00 UTC on 2018-04-14, when B0950+08 was within the detection region of the image ( $\sim 50^\circ$  from zenith). This resulted in the light curves illustrated in Fig. 5.

In order to discern the behaviour of the pulses at lower flux density levels, a correction must be made to remove the variability of the background. At low radio frequencies the background sky appears with a nonzero flux (positive or negative), and variability correlated over a  $\sim 10$  minutes (see Sect. 2 and Kuniack et al. 2018). The light curve shown on the bottom left side of Fig. 5 illustrates the forced flux measurements at a location on the sky, a few beam widths away from B0950+08, where no sources visible to AARTFAAC are present. This background was then subtracted, shown on the bottom right side of Fig. 5, by modelling the variability with a rolling boxcar mean, with a width of two minutes. Two minutes was short enough to adequately remove the correlated variability, and long enough that EFPs do not significantly dominate the rolling mean. The result of subtracting the boxcar mean is shown in the right side of Fig. 5. The top panels show the result of the same procedure applied to the location of B0950+08. The statistics of the background light curve are fit very well by a Gaussian distribution. In contrast, the background subtracted light curve of B0950+08 (top right of Fig. 5) is highly skewed above the mean flux density by many more EFPs than previously detected.

Figure 6 shows the depth to which AARTFAAC is able to probe the fluence distribution of B0950+08 emission compared to the background. Each plot depicts the population of pulses detected in the transient candidate database via the blind search criteria, compared to the distribution of flux measurements made every second at the location of the pulsar and the nearby background. We find that it is possible to resolve a break in the power law below the  $5\sigma$  sensitivity limit of the blind detection pipeline. This break

is significantly higher than the variance of the background. The Astropy smooth broken power-law model was fit to the cumulative distribution with fluence ratio greater than 300 (where the pulsar curve was still an order of magnitude greater than the background curve), using the SciPy function `curve_fit` (Jones et al. 01). The fluence to MIP fluence ratio of the power-law breaks occur at around 453 for 58.3 MHz and 861 for 61.8 MHz, corresponding to fluences of approximately 25 Jy s, and 48 Jy s, respectively. The location of the break between the two power-laws is highly dependent on the smoothing factor. In this case the range of the smoothness parameter  $\delta$  fit was bound to 0.25. This bound was chosen because it ensured that all other parameters were fit freely, and upon visual inspection the function describes the data well. The power-law indices on either side of the break are printed on either side of the grey dashed line.

### 3.2 Pulse clustering

The clustering of time series can be measured in two ways, both by comparing to what would be expected from a Poisson process. First, the dispersion index, the ratio of the variance to the mean of binned arrival times. A dispersion index of 1 is expected for a Poisson process, less than one is overly regular data, and greater than one for clustered data. Unfortunately, this has the drawback of being dependent on the width of the bins used. However, for all reasonably sized bins (30 seconds to 10 minutes) the dispersion index is greater than 1 during the two most active days, see Fig. 7, indicating a greater tendency for giant pulses to appear in clusters. Secondly, the clustering can be measured by comparing the pulse inter-arrival times, the interval of time between each pulse. For a Poisson process the distribution of inter-arrival times should be exponential. Likewise, the distribution of inter-arrival times was not well fit by an exponential distribution. Instead, there was a greater number of short inter-arrival times, illustrated in the left plot of Fig. 8.

However, following the reprocessing of 2018-04-14, described in Section 3.1.1, pulse clusters could be seen to follow peaks in the correlated variability of the background, see left side of Fig. 5. Removing this modulation in the background flux density and sensitivity eliminated the  $\sim 10$  minute clusters. The corrected distribution of pulse inter-arrival times is shown in the right plot of Fig. 8, and clearly follows an exponential decay in the rate of pulses as inter-arrival time increases, agreeing well with Poisson statistics.

Note however, that this agreement with Poisson statistics is limited to the duration of the individual observation, Fig. 1 shows the strong variability in the rate of detected pulses over the months spanned by our data, which cannot be explained by sensitivity variations.

### 3.3 Pulse spectral behaviour

In order to inspect the spectral structure of the EFPs, we re-imaged the 16, 195.3 kHz sub-bands separately. The observation was on 2018-04-14, the date with the largest number of observed pulses. All of the pulses detected in the blind search mode are plotted in the top panel of Fig. 7. 40 of the brightest pulses spanning 18:23 to 21:01 UTC are illustrated in Fig. 9. The image stamps have a consistent colour scaling,

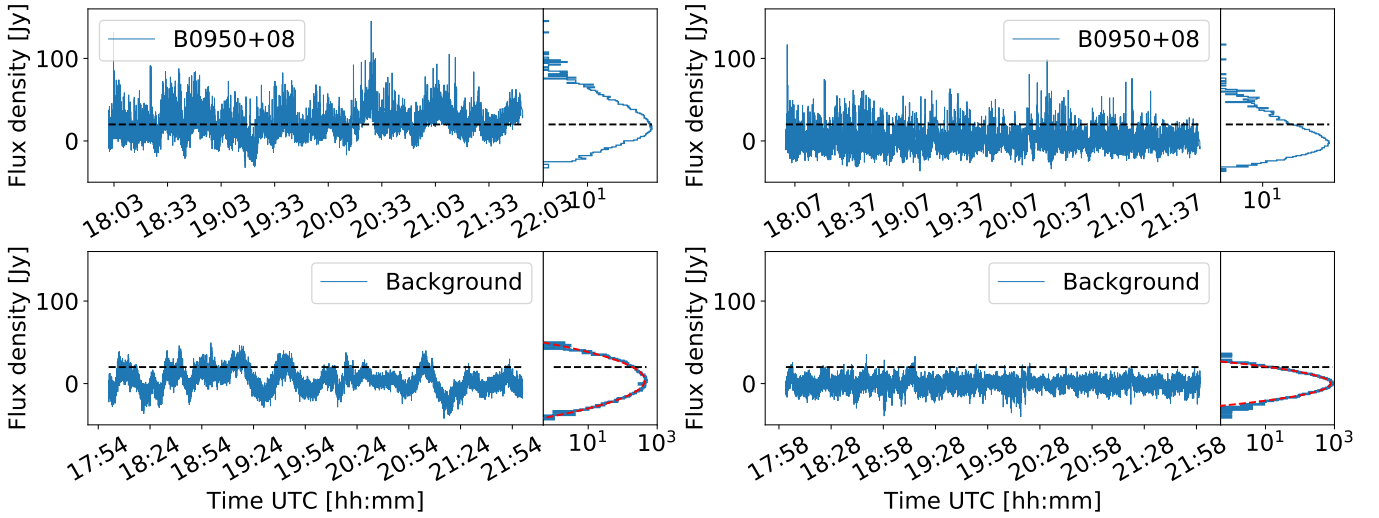


**Figure 5.** Fully sampled light-curve of B0950+08 (top) and a nearby background location (bottom). Both light curves on the left show correlated noise variations which have been removed with a two minute boxcar rolling mean. The black dashed line shows the mean of the B0950+08 light curve, prior to background subtraction, in all four plots. The red dashed line on the histograms of both bottom plots illustrates how well the background is described by a Gaussian.

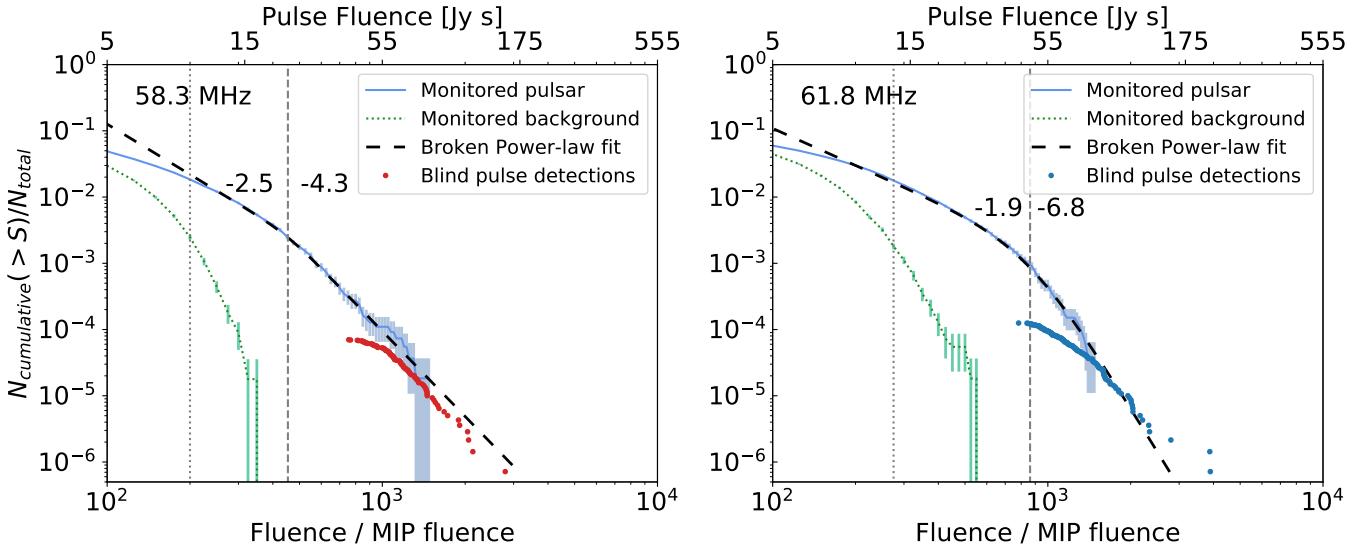


**Figure 6.** Extending the distribution of extreme-fluence pulses to lower fluences using the monitoring measurements from Fig. 5, for 58.3 MHz (left) and 61.8 MHz (right). As in Fig. 3, the horizontal axis is normalised to the mean fluence of typical pulses, and the vertical axis to the total number of rotation periods in the measured time interval. The dots show the pulses detected in the blind search, copied from Fig. 3. The pulse fluence distribution from monitoring is shown in light blue (with Poisson error bars) and the background fluence distribution is shown in green (again with Poisson error bars). The black dashed line shows a broken power-law model to the overall pulse fluence distribution, with the grey vertical dashed line indicating the location of the break, and the numbers to either side of it the asymptotic low- and high- fluence power-law indices. The grey dotted line shows the point above which the background contributes less than 10% to the distribution.

and provide a qualitative comparison of the relative flux in each frequency channel. The stamps are separated vertically according to the clusters of time, and horizontally in the two consecutive sequences of sub-bands.

Interestingly, we find that the spectra of the pulses are highly structured and variable, with many narrow band pulses, and with pulses close in time tending to have similar structure.

## 4 DISCUSSION

### 4.1 Pulse fluence

Being so nearby, the DM for PSR B0950+08 is  $\sim 3 \text{ pc cm}^{-3}$ . This leads to a dispersion delay between the two AART-FAAC images, 1.5 MHz bandwidth centered at 58.3 and 61.8 MHz, of 0.4 seconds. Given the rotation period is  $\sim 0.25$  seconds, a pulse appearing split between two time

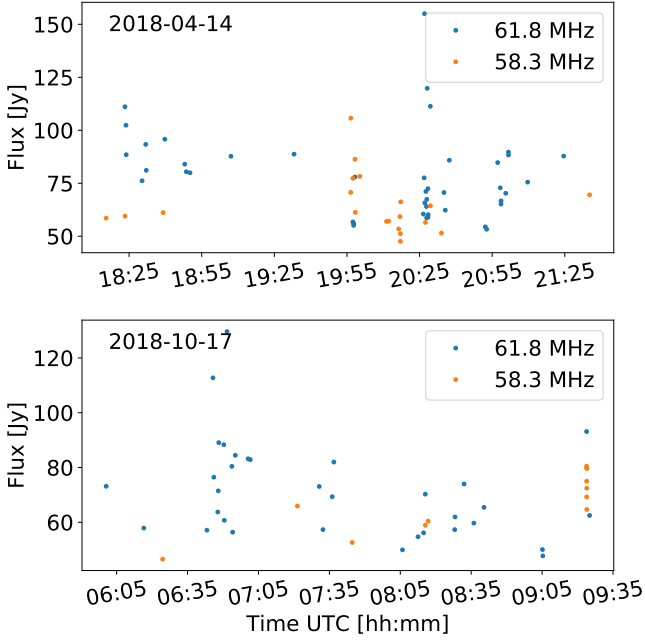


**Figure 7.** Pulse arrival times, coloured by the detection frequency from the two most active days. The dispersion index measured for a range of bin time bin widths is greater than 1, indicating that the pulse behaviour is clustered more than expected from a Poisson process.

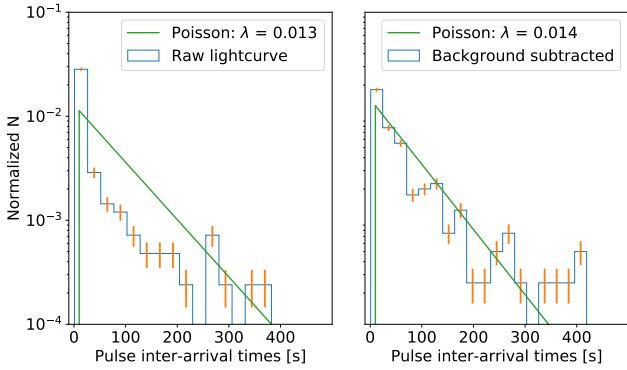


**Figure 8.** Histograms of the inter-arrival times for pulses greater than 50 Jy. Counting uncertainty is the square root of the number of counts. The left panel shows the distribution for the raw light curve, and the right for the background subtracted light curve. The raw light curve is over clustered, whereas once the background is removed, the distribution follows an exponential decay, indicative of a Poisson process.

steps must necessarily come from a single pulse event. Estimation of the pulse fluence requires evidence that the emission in an AARTFAAC image comes from a single pulse. Because pulse signals arriving in the higher frequency image before the lower frequency image have been observed in a number of cases, and that these pulses split in time bins are not different in fluence level than the total population, we can be confident that the majority of measured pulses are individual pulses.

The LWA papers (Tsai et al. 2015, 2016), referred to

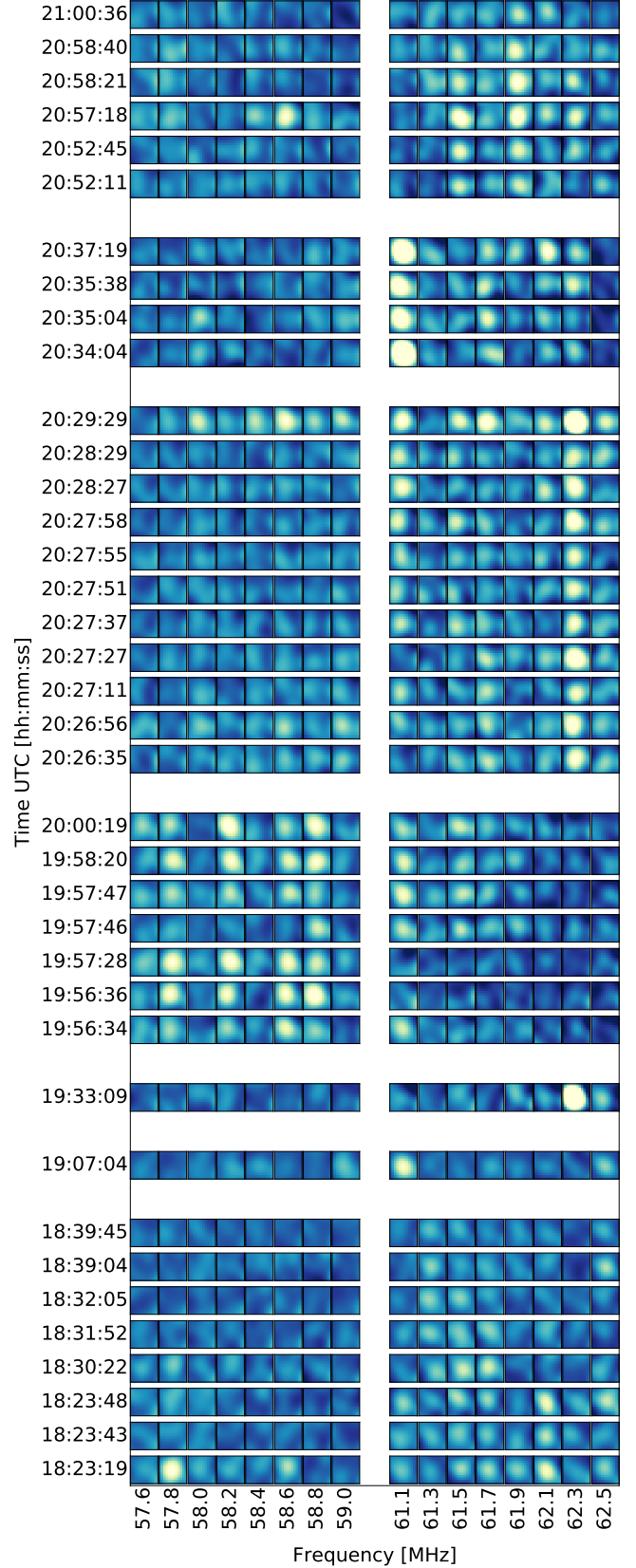


**Figure 9.** Time/frequency plot of the brightest pulses from 2.5 hours on 2018-04-14. It is clear that the spectral structure is not the result of DISS, which has a bandwidth of  $\approx 65$  kHz and would average out over only a few of the 195.3 kHz sub-bands.

for comparison in Table 1, resolve the pulse profiles of the giant pulses. Given that sampling with a finer time resolution than the width of the pulse causes flux to be spread across multiple time bins, the peak flux densities reported are not equivalent to total pulse fluences, as is the case in the temporally unresolved giant pulses at 112 MHz (Smirnova 2012), and AARTFAAC.

Therefore, extracting a peak flux from a 1 second integrated image requires an assumption about the burst profile. For B0950+08, the histogram of all giant pulse widths observed (Figure 9; Tsai et al. 2015) shows that nearly all giant pulses have a FWHM less than the MIP. The MIP widths measured by Tsai et al. (2016) were 25.6 ms and 17.8 ms at 42 MHz and 74 MHz, respectively. Furthermore, Kazantsev & Potapov (2018) showed that for many different pulsars which produced giant pulses at 111 MHz, a giant pulse typically has a much narrower width compared the MIPs. Of the strongest pulses from each of the eight pulsars observed to produce giant pulses, none were resolved at their time resolution of 1.2288 ms. Additionally, using the Westerbork Synthesis Radio Telescope (WSRT) Singal & Vats (2012) show an example giant pulse with a width of less than one millisecond. If this is the case for the AARTFAAC pulses this would imply an extremely large peak flux and make comparison between studies impossible. Importantly, this could explain why pulses this large were not observed by the LWA, as these would likely have been flagged as radio frequency interference (RFI) by their pipeline. Typically extremely bright and narrow band signals are flagged.

Therefore, in order to compare the results of this work with previous giant pulse studies, pulse fluences were used as a consistent unit, since that is what is directly measured when the pulse is unresolved. This required an assumption about the intrinsic pulse width in order to use results from LWA. From the population of pulse widths shown in (Figure 9 Tsai et al. 2015), we can see that the giant pulses recorded follow a roughly flat distribution, from the lower pulse width limit of 5 ms (a lower limit imposed during the single pulse search by Tsai et al. (2015, 2016)) to the MIP width of 30 ms, we can therefore use their reported average of 17.8 ms, which is roughly half the MIP width. Lastly, the giant pulse peak, and the MIP fluence, width, and peak values, calculated by interpolation, are given for comparison in Table 1.

## 4.2 Fluence magnitude discrepancy

The fact that we observe pulses that are about 100× brighter than pulses which have been previously reported by a similar instrument, at a similar frequency raises an interesting question: why? The pulses must be intrinsically emitted with a greater energy, or extrinsically magnified during propagation.

### 4.2.1 Magnification during propagation

It has been shown in previous studies of B0950+08 (Gupta et al. 1993; Singal & Vats 2012) that the MIP amplitude can vary by up to an order of magnitude over the course of a few days. This form of pulse magnification, refractive interstellar scintillation (RISS), causes variability on timescales of days. Without being able to measure the MIP during

each observation, we are unable to determine the relative magnitude difference between the pulses we observe and the MIP from one day to the next. This could be accomplished with AARTFAAC detecting a period of high activity from PSR B0950+08, then triggering a simultaneous observation with higher sensitivity and time resolution, or by comparing the archived AARTFAAC observations with contemporaneous observations from another instrument. Nevertheless, the maximum magnification factor (10×) of RISS is not large enough to explain the difference between what we observe and the LWA results.

In addition to RISS, pulsar signal is also diffracted by the interstellar medium during propagation (DISS). Bell et al. (2016) recently measured a DISS bandwidth of 4.1 MHz and timescale of 28.8 minutes at 154 MHz using the MWA. These values agree well with a previous study at 50 MHz by Phillips & Clegg (1992), indicating the dynamics of the interstellar medium have been stable over the last three decades. Applying the scaling relations for bandwidth  $\Delta\nu_d \propto \nu^{4.4}$ , and timescale  $\Delta\tau_d \propto \nu^{1.2}$ , to their results predict, at 60 MHz, a bandwidth of 65 kHz and timescale of 10.3 minutes. The spectral energy distribution across the 16 AARTFAAC frequency bands from the brightest pulses from 2018 April 14 are shown in Fig. 9. Spectral structures, caused by scintillation, or 'scintels', with a bandwidth of 65 kHz, would be expected to average out after a few times the scintillation bandwidth. Therefore, intrinsically broadband pulses, modulated by DISS should appear broadband when integrating more than two AARTFAAC sub-bands, each being 195.3 kHz wide. This indicates that the structures present in Fig. 9 are not scintels but intrinsically narrow band emission. However, it can be seen that the frequency structures are not varying significantly on timescales less than 10 minutes, the predicted scintillation timescale. It is therefore likely that the emission is intrinsically narrow band, but is still modulated by the ionosphere and interstellar medium.

Recently Main et al. (2018) showed that pulses emitted from PSR B1957+20 can be lensed by ionized gas, blown off of its binary companion by the pulsar wind. While the pulses observed by AARTFAAC may not be clustered in time within the span of a single active observation, the activity is extremely clustered day-to-day. This could imply that a highly clumped turbulent screen is passing across the line of sight. Precise measurements of the differential DM or rotation measure during days of high activity and low activity might reveal variations in the ISM. Regardless, there is no evidence for a binary companion or debris disc around B0950+08 (Wang et al. 2014), and the maximum magnification factor measured by Main et al. (2018) was only 30×, much less than what what is required to explain the luminosity of the pulses we have detected.

### 4.2.2 Intrinsic emission

Zhuravlev et al. (2013) shows a break in the power law between the cumulative probability distributions of GPs from B1937+21. The index changes from  $-1.6 \pm 0.1$  at lower flux levels to  $-2.4 \pm 0.1$  at the higher flux tail. This is similar to the behaviour observed by Popov & Stappers (2007) who also show that giant pulses from the Crab pulsar have a break in the power law, the higher flux tail is steeper than the low flux tail. Oddly, the opposite was observed in the



distribution of giant pulses observed from the same pulsar by McKee et al. (2019) where the distribution flattens significantly, from  $-3.48 \pm 0.04$  to  $-2.10 \pm 0.02$ , at the high flux tail.

Interestingly, when searching for giant pulses, Kazantsev & Potapov (2018) found that the typical pulse energy distribution for B0329+54 was clearly best fit by a broken power law, despite not detecting any giant pulses from this pulsar. It was the only pulsar monitored which exhibited this behavior.

The similarity in shape of the flux distributions, to emission observed from other pulsars emitting giant pulses provides strong evidence that the signal we are observing is intrinsic to the pulsar, rather than being the result of propagation effects.

Furthermore, we note that the frequency structure of the individual pulses shown in Fig. 9 are similar in character to the single pulse spectra shown in other studies of giant pulses, from different pulsars, at different frequencies. This sparse comb-like structure is observed from B1957+20 between 338 and 324 MHz (Main et al. 2017), B1821-24A between 720 and 2400 MHz (Bilous et al. 2015), and from B1937+21 between 1332 and 1450 MHz (McKee et al. 2019). These GP spectra are different in nature to the MIP spectra, which appear to be broadband signals modulated by interstellar scintillation (ISS). However, it must be noted that MIPs are by definition averaged over many pulse periods. Whether a single typical pulse exhibits a similar frequency structure is unknown.

Lastly, the recent radio outburst from the magnetar XTE J1810-197, allowed for the spectral properties to be studied (Maan et al. 2019). Interestingly, the bursts exhibited high spectral modulation on frequency scales much greater than the scintillation bandwidths, which were then observed to evolve and dissipate in the months after the initial outburst.

Given that B0950+08 has a relatively low magnetic field, and magnetars have fields stronger than  $10^{14}$  G, similarity in the emission characteristics would be interesting. Unfortunately, the coarse frequency resolution of AARTFAAC, and being limited to only detecting the brightest pulses, makes a study of the evolution of the spectral modulation during periods of high activity and quiescence impossible. However, follow up observations with the full LOFAR array could elucidate any further similarities between the pulses we observe from B0950+08 and the outburst from XTE J1810-197.

### 4.3 Pulse rate discrepancy

Lastly, we discuss the question of why previous single pulse surveys of this particular pulsar, at similar radio frequencies, and with an instrument of a similar design, did not detect pulses with a similar fluence magnitude.

Of the 96 hours, or 42 observations, which we have used to search for detectable pulses, 18 observations, totalling 37 hours, contained no detectable pulses. Assuming the activity level is typical this indicates that roughly 40% of observations could yield no pulses at this extreme fluence level. However, in 21 of our observations the rate of detected pulses was greater than one per hour. Therefore, if this extreme activity is equally likely on any given day, the LWA surveys, whose

observations were composed of 6 hour blocks over 5 days Tsai et al. (2015), then 4 hour blocks over 3 consecutive days (Tsai et al. 2016), should have observed pulses of a similar magnitude. There is only a 6% chance to randomly select 8 observations which contain no pulses.

However, the LWA observations were not randomly selected; they took place over consecutive days. This could indicate that the activity level is clustered on timescales of weeks or greater. Unfortunately, due to the irregular distribution of our observations we are unable to determine the degree to which EFP activity is clustered over timescales of weeks or months.

Recently, a follow-up study utilizing an additional 26 hours of observations, simply monitoring the location of B0950+08 with a  $5\sigma$  detection threshold, daily from 2019 September 1<sup>st</sup> to 8<sup>th</sup>, as well as the 10<sup>th</sup>, 11<sup>th</sup>, 14<sup>th</sup>, 15<sup>th</sup>, and 18<sup>th</sup>, yielded no pulses. This indicates that there are long periods of quiescence between storms of extreme pulse activity. With the observations where pulses were detected, we may simply have caught unique periods of high energy output. This would explain why the relatively few observations performed by LWA over consecutive days resulted in no similarly extreme pulses. Additionally, it is worth noting again that extremely bright, narrow band signal, is typically flagged automatically during RFI mitigation.

## 5 CONCLUSIONS

We report on the observation of a population of extremely high fluence pulses from B0950+08. These pulses achieve a fluence more than two orders of magnitude brighter than any which have previously been observed at similar low radio frequencies. Interestingly, though the power-law index of the fluence distribution is well predicted by the previous studies' by Tsai et al. (2015, 2016), the total rate of pulses at the brightness we observe is much greater than would be expected continuing the previous studies distribution to these fluences.

As a result, the distribution observed here cannot be extended to the flux range of the typical pulses. The population must therefore have a low flux turn-over which separates this population from the typical pulses. By reprocessing the observation, monitoring the position of the pulsar, and subtracting background variability, we were able to extend the population of pulse measurements below the transient surveys  $5\sigma$  detection limit. This revealed the pulse flux distribution follows a broken power law, with the breaks occurring around 25 Jy s and 48 Jy s, at 58.3 and 61.8 MHz. We also found that the shape of the bright end of this distribution was consistent between observations spanning several months, as well as a range in extreme pulse activity.

Lastly, alternative explanations for the extreme fluence were considered. Whether we are observing a different pulse mechanism producing intrinsically brighter pulses, or whether propagation effects are magnifying the pulses. Using the 16, 195.3 kHz sub-bands available to AARTFAAC we analyzed the spectral properties of the brightest pulses during a period of high activity. We found that the pulses exhibit highly modulated spectra, with characteristics very different to what would be expected from intrinsically broadband signal modulated by interstellar scintillation. Within

the observed bandwidth, sparse and narrow band structures, reminiscent of spectra observed from other giant pulses are clearly visible. Furthermore, the magnification factor required to reconcile the discrepancy between our population and those previously reported is much greater than what has been observed from a plasma lens, or the ISM. Therefore the explanation that we are observing a mechanism producing pulses which are intrinsically much more luminous is clearly favoured.

## ACKNOWLEDGEMENTS

AARTFAAC development and construction was funded by the ERC under the Advanced Investigator grant no. 247295 awarded to Prof. Ralph Wijers, University of Amsterdam; This work was funded by the Netherlands Organisation for Scientific Research under grant no. 184.033.109. We thank The Netherlands Institute for Radio Astronomy (ASTRON) for support provided in carrying out the commissioning observations. AARTFAAC is maintained and operated jointly by ASTRON and the University of Amsterdam.

We would also like to thank the LOFAR science support for their assistance in obtaining and processing the data used in this work. We use data obtained from LOFAR, the Low Frequency Array designed and constructed by ASTRON, which has facilities in several countries, that are owned by various parties (each with their own funding sources), and that are collectively operated by the International LOFAR Telescope (ILT) foundation under a joint scientific policy.

Additionally we express gratitude to Jason Hessels and Joel Weisberg for comments on this article, as well as Joanna Rankin and Mathew Bailes for invaluable discussion. And to Jean-Mathias Griessmeier and Louis Bondonneau for sharing illuminating data on the typical pulse behaviour of B0950+08.

This research made use of Astropy,<sup>4</sup> a community-developed core Python package for Astronomy (Astropy Collaboration et al. 2013; Price-Whelan et al. 2018), as well as the following: KERN (Molenaar & Smirnov 2018), Pandas (McKinney 2010), NumPy (van der Walt et al. 2011), SciPy (Jones et al. 01), and corner.py (Foreman-Mackey 2016). Accordingly, we would like to thank the scientific software development community, without whom this work would not be possible.

## REFERENCES

- Astropy Collaboration et al., 2013, *A&A*, **558**, A33
- Bell M. E., et al., 2016, *Monthly Notices of the Royal Astronomical Society*, **461**, 908
- Bilous A. V., Pennucci T. T., Demorest P., Ransom S. M., 2015, *ApJ*, **803**, 83
- Brisken W. F., Benson J. M., Goss W. M., Thorsett S. E., 2002, *ApJ*, **571**, 906
- Cairns I. H., 2004, *The Astrophysical Journal*, **610**, 948
- Foreman-Mackey D., 2016, *The Journal of Open Source Software*, **24**
- Gupta Y., Rickett B. J., Coles W. A., 1993, *ApJ*, **403**, 183
- Hewish A., Bell S. J., Pilkington J. D. H., Scott P. F., Collins R. A., 1968, *Nature*, **217**, 709
- Jones E., Oliphant T., Peterson P., et al., 2001–, SciPy: Open source scientific tools for Python, <http://www.scipy.org/>
- Kazantsev A. N., Potapov V. A., 2018, *Research in Astronomy and Astrophysics*, **18**, 097
- Kazantsev A. N., Potapov V. A., Safronov G. B., 2019, *Astronomy Reports*, **63**, 134
- Kuiack M., Huizinga F., Molenaar G., Prasad P., Rowlinson A., Wijers R. A. M. J., 2018, *Monthly Notices of the Royal Astronomical Society*, **482**, 2502
- Kuzmin A. D., 2007, *Ap&SS*, **308**, 563
- Maan Y., Joshi B. C., Surnis M. P., Bagchi M., Manoharan P. K., 2019, arXiv e-prints, p. [arXiv:1908.04304](https://arxiv.org/abs/1908.04304)
- Main R., van Kerkwijk M. H., 2018, in Weltevrede P., Perera B. B. P., Preston L. L., Sanidas S., eds, *IAU Symposium Vol. 337, Pulsar Astrophysics the Next Fifty Years*. pp 83–83 ([arXiv:1709.09179](https://arxiv.org/abs/1709.09179)), doi:[10.1017/S1743921317009176](https://doi.org/10.1017/S1743921317009176)
- Main R., van Kerkwijk M., Pen U.-L., Mahajan N., Vanderlinde K., 2017, *ApJ*, **840**, L15
- Main R., et al., 2018, *Nature*, **557**, 522
- Manchester R. N., Hobbs G. B., Teoh A., Hobbs M., 2005, *AJ*, **129**, 1993
- McKee J. W., et al., 2019, *MNRAS*, **483**, 4784
- McKinney W., 2010, in van der Walt S., Millman J., eds, *Proceedings of the 9th Python in Science Conference*. pp 51 – 56
- Molenaar G., Smirnov O., 2018, *Astronomy and Computing*
- Phillips J. A., Clegg A. W., 1992, *Nature*, **360**, 137
- Popov M. V., Stappers B., 2007, *A&A*, **470**, 1003
- Prasad P., Wijnholds S. J., Huizinga F., Wijers R. A. M. J., 2014, *A&A*, **568**, A48
- Prasad P., et al., 2016, *Journal of Astronomical Instrumentation*, **5**, 1641008
- Price-Whelan A. M., et al., 2018, *AJ*, **156**, 123
- Singal A. K., 2001, *Ap&SS*, **278**, 61
- Singal A. K., Vats H. O., 2012, *AJ*, **144**, 155
- Smirnova T. V., 2012, *Astronomy Reports*, **56**, 430
- Spangler S. R., 2009, *Space Sci. Rev.*, **143**, 277
- Staelin D. H., Reifstein Edward C. I., 1968, *Science*, **162**, 1481
- Swinbank J. D., et al., 2015, *Astronomy and Computing*, **11**, 25
- Tsai J.-W., et al., 2015, *The Astronomical Journal*, **149**, 65
- Tsai J.-W., Simonetti J. H., Akukwe B., Bear B., Gough J. D., Shawhan P., Kavic M., 2016, *The Astronomical Journal*, **151**, 28
- Wang N., Manchester R. N., Johnston S., Rickett B., Zhang J., Yusup A., Chen M., 2005, *MNRAS*, **358**, 270
- Wang Z., Ng C. Y., Wang X., Li A., Kaplan D. L., 2014, *ApJ*, **793**, 89
- Wang W., Lu J., Zhang S., Chen X., Luo R., Xu R., 2019, *Science China Physics, Mechanics, and Astronomy*, **62**, 979511
- Zhuravlev V. I., Popov M. V., Soglasnov V. A., Kondrat'ev V. I., Kovalev Y. Y., Bartel N., Ghigo F., 2013, *MNRAS*, **430**, 2815
- van Haarlem M. P., et al., 2013, *A&A*, **556**, A2
- van der Walt S., Colbert S. C., Varoquaux G., 2011, *Computing in Science and Engineering*, **13**, 22

This paper has been typeset from a  $\text{\TeX}/\text{\LaTeX}$  file prepared by the author.

<sup>4</sup> <http://www.astropy.org>